Rev.Adv.Mater.Sci. 5 (2003) 403-412

EFFECTS OF TOPOGRAPHY IN NANO-STRUCTURED THIN FILMS: A LORENTZ TRANSMISSION ELECTRON MICROSCOPY AND ELECTRON HOLOGRAPHY STUDY

Jeff Th. M. De Hosson and Hans A. De Raedt

Department of Applied Physics, Materials Science Centre and Netherlands Institute for Metals Research, University of Groningen, Nijenborgh 4, 9747 AG Groningen, The Netherlands

Received: August 14, 2003

Abstract. This paper aims at applying advanced transmission electron microscopy (TEM) to functional materials, such as ultra-soft magnetic films for high-frequency inductors, to reveal the structure-property relationship. The ultimate goal is to delineate a more quantitative way to obtain information of the magnetic induction and local magnetization. Nano-crystalline Fe-Zr-N films have been prepared by DC magnetron reactive sputtering with a thickness between 50 and 500 nm. Conventional TEM and selected area diffraction (SAD), reveal crystallites of sizes ranging between 2 and 30 nm. The films showed a granular or hillock type of roughness with an rms amplitude of 5 nm. In particular this paper concentrates on an analysis of phase maps in electron holography and intensity maps in Lorentz transmission electron microscopy including the thickness variation over the sample. For a particular statistical description of the roughness and values for the roughness it is shown that analytical expressions can be obtained. We demonstrate that starting from the concept of the vector potential in classical electrodynamics these results can be achieved assuming independent stationary Gaussian distributions for the height correlation functions.

1. INTRODUCTION

Deviations of thin film interfaces from flatness may have a substantial effect on the functional properties of materials, e.g. magnetic coercive field, demagnetizing field, giant magetoresistance and domain walls [1-4]. Recently the effects of roughness on magnetic properties have been examined by describing the roughness in terms of a self-affine fractal scaling but these studies are focused on the theoretical description rather than on an experimental validation. This paper concentrates on the application of transmission electron microscopy to functional materials, such as ultra-soft magnetic films for high-frequency inductors, to reveal the structure-property relationship. There exists an increasing demand for further miniaturization in portable appliances (e.g. mobile phones, palmtops), that is to say in communication tools. To this end the use of high-frequencies (e.g. 10-1000 MHz) in combination with thin magnetic materials is desirable. The use of magnetic films allows the integration of transformers and inductors into silicon IC circuitry. Further, soft-magnetic films are also widely used in modern electromagnetic devices as a high-frequency (>100 MHz) field-amplifying component, e.g. in read-write heads for magnetic disk memories for computers and as a magnetic shielding material, e.g. in turners. The main requirements for the film material are: a high saturation magnetization, combined with a low coercivity and a small but finite anisotropy field. In addition the material should have a reasonably high specific electrical resistivity to reduce eddy currents, and also appropriate mechanical properties. To obtain the desired properties (low coercivity, little strain and very small magnetostriction) the use

Corresponding author: Jeff Th. M. De Hosson, e-mail: hossonj@phys.rug.nl

materials with grain size of the order of 10 nm nanometers, like nano-crystalline iron based materials, becomes attractive.

Knowledge of local magnetic properties is essential for the development of new magnetic nanosized materials. One of technique that is suitable for the measurement of local magnetic structures is Lorentz-Fresnel (or defocused) imaging mode of transmission electron microscopy. This rather classical TEM technique [5,6] has several outstanding advantages: uncomplicated application to various parts of thin foil, possibility of dynamical studies and good spatial resolution. Nevertheless, to obtain quantitative information from Lorentz micrographs is relatively difficult due to in-direct link between image contrast and spatial variation of magnetic induction, which is problematic in regions of abrupt magnetization changes [7].

In this paper the possibility of a quantitative analysis of the magnetic properties of nano-crystalline iron using transmission electron microscopy is presented taking into account the thickness variation over the area of observation. The ultimate goal is to delineate a more quantitative way to obtain information of the magnetic induction and local magnetization. In particular the latter physical quantities affect the functional properties of ultra-soft magnetic materials for high-frequency inductors. One of the magnetic features that can provide quantitative magnetic information are the so-called magnetization or magnetic ripples, caused by local variation of magnetic induction that deviate from the mean magnetization direction [8]. An alternative transmission electron microscopy technique for obtaining information of the magnetization is electron holography, which is based on recording an interference pattern from which both the amplitude and phase of an object can be reconstructed [9-11]. In this paper a few observations of nano-structured soft-magnetic materials with Lorentz Fresnel (LTEM) and (off-axis) electron holographic techniques are presented (see also [12] and [13]) but the main emphasis is to provide a more rigorous mathematical framework to analyze TEM observations as a function of the topography.

2. EXPERIMENTS AND RESULTS

Nano-crystalline Fe-Zr-N films have been prepared by DC magnetron reactive sputtering with a thickness between 50 and 1000 nm. The presence of zirconium is to catch the nitrogen in the iron matrix. Iron was chosen because it is easy to prepare and cheaper than other soft magnetic materials, e.g. cobalt. The nitrogen is added to get a small (nanosized) grain size. Pure (99.96 at.%) Fe sheets partially covered with Zr wires were used as targets. Varying the sputter power and/or the Ar/N_2 gas mixture controls the N and Zr contents. An 800 Oe magnetic field was applied in the plane of the samples during deposition. More details on the film deposition can be found in [14-16].

The films have been deposited on a glass or silicon substrates at several temperatures between room temperature and 200 °C. The DC-sputtered samples were deposited on either a silicon substrate covered by a polymer, which was removed in acetone after sputtering, or on a silicon substrate covered by a Si_3N_4 layer. The former samples were extracted on copper TEM-grids for support, while the latter samples kept their substrate because the layers were very thin. The deposition conditions were chosen to obtain a composition $(Fe_{99}Zr_1)_{1-x}N_x$, where the concentration of nitrogen was in the range $x \leq 25$ at.%. The best films as far as nano-size dimensions are concerned have been obtained for 8 at.%<x<20 at.%. The nitrogen concentration has been measured with Elastic Recoil Detection technique, Neutron Depth Profiling methods and compared with shifts in the XRD pattern. Standard θ-2θ XRD scans showed that up to x=10 at.% as sputtered films were bcc single-phase materials with a strong (110) fiber texture. The grain size, estimated from the width of the (110) peak decreased monotonically with N content from typically 100 nm in the case of N-free films to less than 10 nm for films containing 8 at.%.

The specimens were examined with a JEOL 2010F 200 kV transmission electron microscope equipped with a post column energy filter (GIF 2000 Gatan Imaging Filter, with a resolution of 1024x1024 pixels), which provides an additional magnification around 20 at the plane of CCD camera with respect to the maximal attainable magnification by using the objective minilens (magnification: $6 \cdot 10^3$). For holography the microscope is mounted with a biprism (JEOL biprism with a 0.6 μm diameter platinum wire). Grain size determination was done with several tilting experiments using an ACT: Automated Crystallography for the TEM, from TSL/EDAX and a Gatan dual-view CCD camera. A single-tilt specimen holder and a double-tilt heating specimen holder were used. The images are acquired and edited using DigitalMicrograph (DM) 3.3 and 3.4. Furthermore an additional script package for DM was used (from the Berkeley NCEM Package Image).

Conventional TEM and selected area diffraction (SAD), reveal a 2-30 nm size of crystallites after

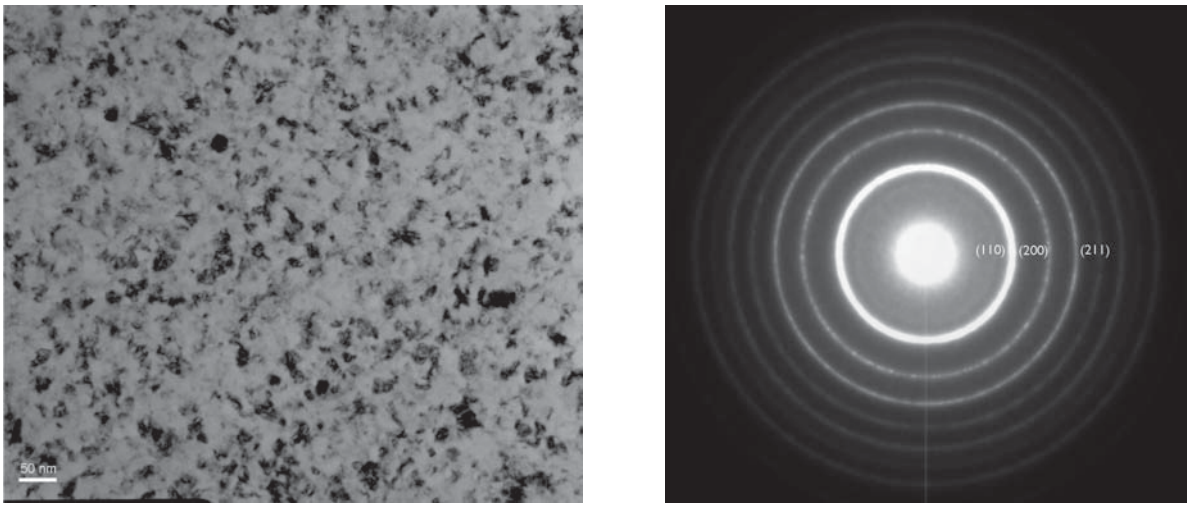

a) **b)**

Fig. 1. (a) Nano-crystalline iron and (b) SA diffraction pattern of nano-crystalline $Fe_{94}N_5Zr_1$.

various tilting experiments for most of the investigated sputter deposited films (see Fig. 1) and in the diffraction pattern of Fig. 1b the allowed reflections for the bcc structure were found (110, 200, 211). No signs of Fe_4N or $Fe_{16}N_2$ were detected in XRD. A very weak ring within the first bright ring can be observed that originates from an oxide layer on the surface. The average measured grain size is approximately 34 nm as shown in Fig. 2. The grain size distribution is rather broad, even for sputtered films. Indeed, one should be careful with this ACT analysis when the film thickness is much larger than the grain size. The information of more grains on top of each other may cause the ACT to measure an incorrect grain size and a different orientation distribution. It should be stressed that the grain size distribution depends on the exact condition of the deposition process, i.e. on the nitrogen concentration.

An example of an LTEM image with a ripple structure is depicted in Fig. 3. The thickness of the film was about 70 nm. The film was deposited on a substrate with a Cu underlayer which had a granular or hillock type of roughness with an rms amplitude of $\sigma = 5$ nm, with the base of the hills between 100-200 nm in size and with the distance between hills around 200 nm, as revealed by AFM scans as shown in Fig. 4. Because the principal magnetization is perpendicular to the magnetic ripple structure within the magnetic domains, magnetic induction vectors can be drawn in the image(s). An example of a crosstie wall is depicted in Fig. 5.

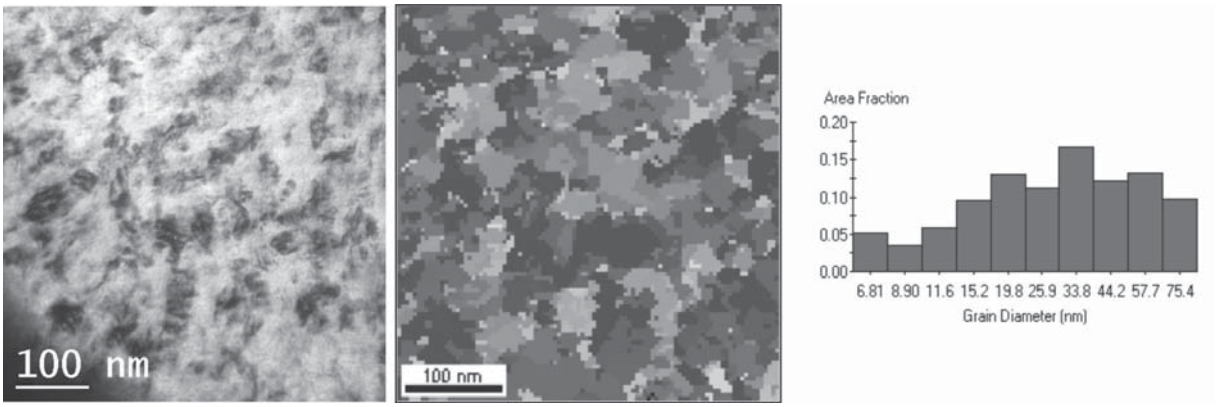

Fig. 2. Grain size and grain size distribution from ACT300 analysis (Automated Crystallography for the TEM, from TSL/EDAX).

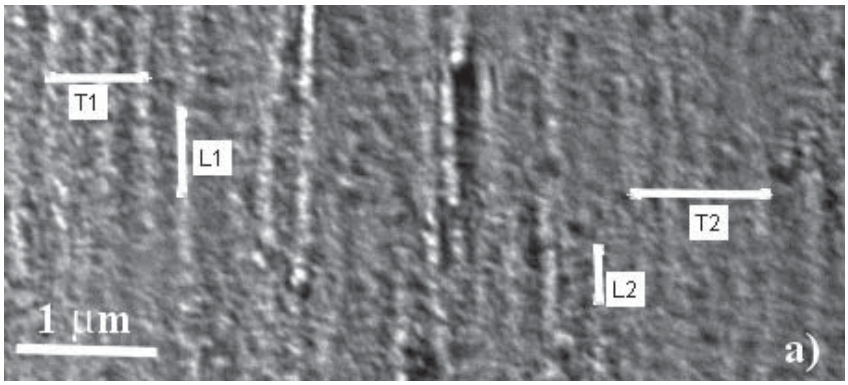

Fig. 3. LTEM image of micromagnetic ripple.

The intensity of the electron beam at the plane of the LTEM image can be evaluated using the Fourier transform technique, e.g. [17,18]:

$$I(\vec{r}) = \left| \int e^{i\varphi(\vec{r}')} e^{ia(\vec{r}-\vec{r}')^2} d\vec{r}' \right|^2, \qquad (1)$$

where $\varphi(\vec{r}')$ represents the phase due to the magnetization and *a* is a constant depending on the defocus value and the wave length (λ_0 = 2.5 pm for the 200 keV-electrons). In Eq. (1) all effects of the aperture and of the spherical aberration in the Fresnel mode of LTEM the transfer function is neglected and a nonzero value of the defocus makes the ripple image observable.

An alternative approach for obtaining information of the magnetization is the use of electron holography. Magnetic thin films are strong phase objects and the phase shift of the electrons passing through the specimen is proportional to the magnetic flux enclosed by the electron paths. There are various, that is to say up to twenty, electron holographic techniques [19], but one of the most popular is off-axis electron holography. The early holograms were limited to the brightness and with that to the coherence of the filament sources. The development of the field emission gun (FEG), which gives a coherent beam with a high intensity, contributed greatly to the implementation of electron holography in practice. For off-axis holography a specimen is chosen that does not completely fill the image plane (for example a small magnetic element or the edge of an extended film) so that only part of the electron beam passes through the specimen. An electrostatic bi-prism, a thin (< 1μm) metallic wire or quartz fiber coated with platinum (or gold), is then used to recombine the specimen beam and the reference

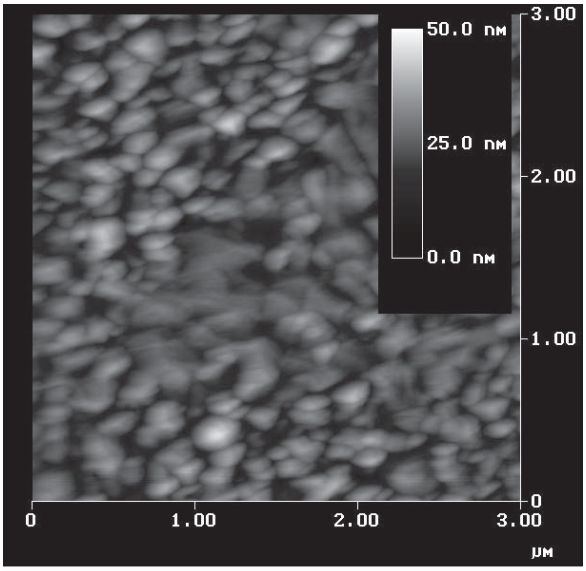

Fig. 4. AFM image of the sputtered film.

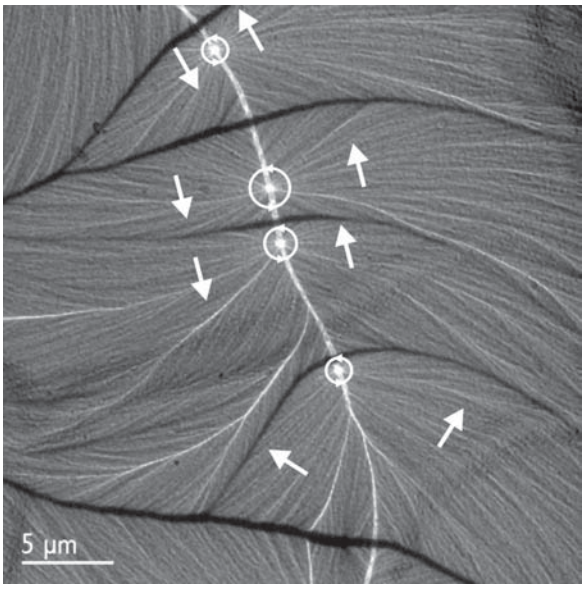

Fig. 5. Magnetization direction in a crosstie wall.

beam so that they interfere and form a hologram. This can be digitized and digital image-processing techniques can be applied to reconstruct an image of the magnetic domain structure. The intensity of the recorded hologram can be written as [11]:

$$I(x,y) = |\Psi_1(x,y)|^2 + |\Psi_2(x,y)|^2 + |\Psi_1(x,y)||\Psi_2(x,y)|\left[e^{i(\varphi_1-\varphi_2)} + e^{-i(\varphi_1-\varphi_2)}\right] = A_1^2 + A_2^2 + 2A_1A_2\cos\Delta\varphi, \quad (2)$$

where Ψ is an electron wave function, φ represents the phase, and the subscripts refer to the reference and object waves, which travel through the opening and the specimen, respectively. Eq. (2) shows that the phase and the amplitude information are encoded in the holographic image. If neither the magnetic induction $\vec{B}$ or the mean crystal potential V vary with the penetration depth z and neglecting magnetic and electric fields outside the sample, then the phase becomes

$$\varphi(x,y) = C_E V(x,y)t(x,y) - \frac{e}{\hbar}\oiint \vec{B}_\perp(x,y)t(x,y)dxdy, \quad (3)$$

where $V(x,y)$ is the mean crystal potential, $t(x,y)$ represents the thickness as a function of the place, $B_\perp$ is the component of the magnetic induction perpendicular to both x and z. Assuming that the thickness is constant over the whole image and the composition is homogeneous, the first right-hand side term drops out and only the second term remains. In summary, provided the phase is fully recovered the derivative of the phase multiplied by a constant will give the magnetic induction as a function of the position in the holographic image.

In Fig. 6 an electron hologram and its (unwrapped) reconstructed phase of the nano-crystalline Fe film is shown. When the phase and the Lorentz Fresnel image of this crosstie wall are compared in Fig. 6, it can be seen that the crossties inside the crosstie wall in both Lorentz Fresnel and holography modes are clearly visible. In Fig. 7 another example of the reconstructed phase of nano-crystalline iron is shown. In this case there is also magnetic contrast outside the sample (light area), which means that there is also a magnetic flux present outside the sample. So far, it should be emphasized that the analysis presented here is restricted to the case of uniform thickness and without any external stray fields. Because of the obvious roughness involved in these nano-structured sputtered films in the following section we will explicitly investigated the influence of the topography.

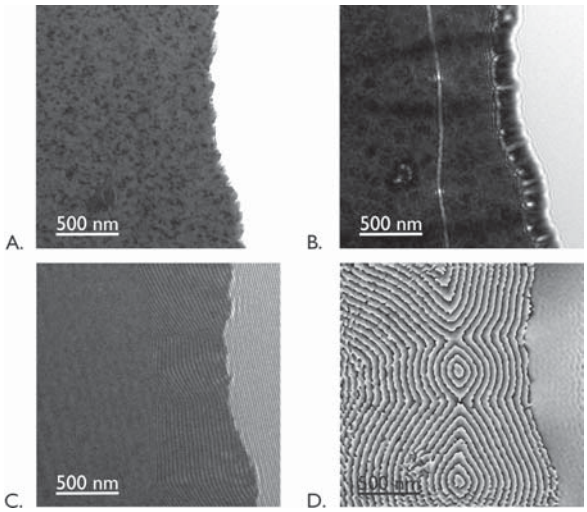

Fig. 6. A structure image (A), a Lorentz Fresnel image (B), a hologram (C) and the reconstructed phase (D) of nano-crystalline $Fe_{94}N_5Zr_1$.

3. THEORETICAL ANALYSIS

Following the theory of Aharonov and Bohm [20], the phase shift between two points of the image is determined by the magnetic flux through the area within lines connecting the corresponding points on the upper and lower surfaces of the films and the trajectories of electrons passing these points, see e.g. [21]. If one of the points is at the origin of the coordinates, we write for the phase shift

$$\varphi(\vec{r}) = \frac{\pi}{\Phi_0}\oiint \vec{B}(\vec{r},t)d\vec{S}, \quad (4)$$

where $\Phi_0 = h/2e = 2.06\cdot10^{-15}$ Wb = 2.06 mT mm^2 is the magnetic flux quantum, e is the electron charge, h is Planck's constant, $\vec{B}$ is the local magnetic induction and $d\vec{S}$ is an element of area, limited by two electron trajectories in consideration, and represented by the vector oriented along the normal to this element. Because we want to include the variation of the thickness t along the electron trajectory, our starting point is the concept of the vector potential $\vec{A}$ whose curl gives $\vec{B}$. According to classical electrodynamics the vector potential can be written in terms of the magnetization $\vec{M}$ [22]:

$$\vec{A}(\vec{r}) = \int_V \frac{\vec{M}(\vec{r}')\times(\vec{r}-\vec{r}')}{|\vec{r}-\vec{r}'|^3}d^3r', \quad (5)$$

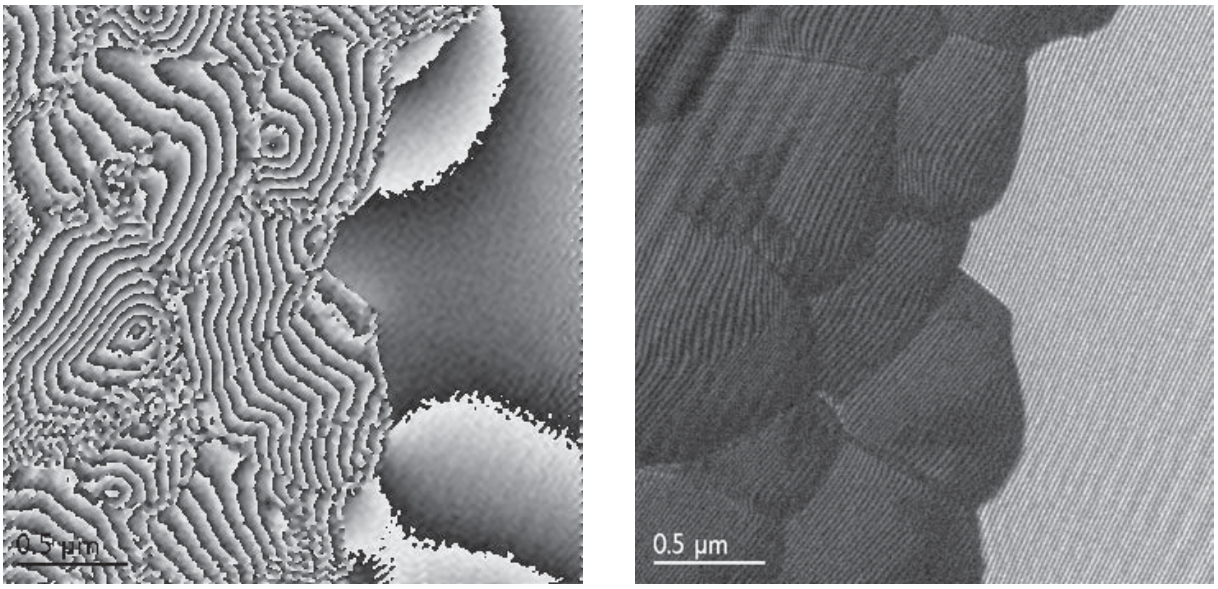

Fig. 7. Hologram (a) and phase image (b) of nano-crystalline $Fe_{94}N_5Zr_1$.

where the integral over the volume V contains the information about the topography of the sample via the volume integral $\int_V d\vec{r}$. In particular the volume of the sample is given by:

$$Volume = \int_{Area} \int dx'dy' \int_{\frac{d}{2}-h_0(x',y')}^{\frac{d}{2}+h_1(x',y')} dz'. \tag{6}$$

The phase is related to the vector potential according to:

$$\varphi(x_i, y_i) = \int_{z_0}^{z_1} A(x_i, y_i, z)dz. \tag{7}$$

where z_0 and z_1 refer to the position of the source and detector, respectively. The phase shift between two points of the image is

$$\varphi(x_0, y_0) - \varphi(x_1, y_1) = \oiint \vec{B}.d\vec{S} + \int_{(x_0,y_0)}^{(x_1,y_1)} \vec{A}(x, y, z_s).d\vec{l} - \int_{(x_0,y_0)}^{(x_1,y_1)} \vec{A}(x, y, z_d).d\vec{l} \tag{8}$$

and it is only identical to the Aharonov and Bohm Eq.(4) *provided* source and detector are positioned far away (i.e. at infinite distance) from the sample. $d\vec{l}$ in Eq.(8) is at constant z-value.

Assuming $\vec{M}(\vec{r}') = M_0\hat{e}_x$ the phase becomes:

$$\varphi(x, y, z_0, z_1) = \int_{z_0}^{z_1} A_z(x, y, z)dz = \int_V \int_{z_0}^{z_1} \frac{M_0(y - y')}{\left[(x - x')^2 + (y - y')^2 + (z - z')^2\right]^{3/2}} dx'dy'dz'dz. \tag{9}$$

Performing the integrals over z and z' we obtain:

$$\varphi(x, y, z_0, z_1) \approx \int dx'dy' \frac{M_0(y - y')(z_0 + z_1 - 2z')}{(x - x')^2 + (y - y')^2} - \int \int_{Area} \left\{1 + \frac{(x - x')^2 + (y - y')^2}{2(z' - z_0)(z_1 - z')}(z_1 - z_0)...\right\}_{z'=-\frac{d}{2}-h_0}^{z'=\frac{d}{2}+h_1}. \tag{10}$$

Eq.(10) is valid if $z_0 << z'$ and $z_1 >> z'$, where z' takes values inside the sample only. If we assume $z_0 = -z_1$ and $|z'| << |z_0|$, up to first order in $1/z_1$ the phase can be written as:

$$\varphi(x, y) = \varphi_0(x, y) + \frac{1}{z_1}\varphi_1(x, y) \tag{11}$$

where:

$$\varphi_0(x, y) = 2M_0 \int_A \int dx'dy' \frac{(y - y')\left[d + h_1(x', y') + h_0(x', y')\right]}{(x - x')^2 + (y - y')^2} \tag{12}$$

and

$$\varphi_1(x,y) = \tag{13}$$
$$2M_0 \int\int_A dx'dy'(y-y')\left[d + h_1(x',y') + h_0(x',y')\right].$$

In the following we use $\vec{r}=(x,y)$ to denote a position in the (x,y) plane and we assume that the surface roughness is described by independent Gaussian random variables $h_0(\vec{r})$ and $h_1(\vec{r}')$ with correlation function $\langle h_i(\vec{r})h_i(\vec{r}')\rangle = \langle h_i(\vec{r}-\vec{r}')h_i(0)\rangle = f(|\vec{r}-\vec{r}'|)$ where the expectation value is taken wih respect to the Gaussian probability distribution.

The intensity of the electron beam at the plane of the LTEM image (see Eq.(1)) can be reformulated so as to include effects of the topography. Eq.(1) is rewritten as:

$$\langle I(\vec{r})\rangle = \iint \left\langle e^{i\left[\varphi(\vec{r}_0)-\varphi(\vec{r}_1)\right]}\right\rangle e^{ia\left[(\vec{r}-\vec{r}_0)^2-(\vec{r}-\vec{r}_1)^2\right]} d\vec{r}_0 d\vec{r}_1 \tag{14}$$

or

$$\langle I(\vec{r})\rangle = \tag{15}$$
$$\iint e^{iB} e^{-\frac{1}{2}\left\langle|\varphi(\vec{r}_0)-\varphi(\vec{r}_1)|^2\right\rangle} e^{ia\left[\vec{r}\cdot(\vec{r}_1-\vec{r}_0)+(\vec{r}_0-\vec{r}_1)\cdot(\vec{r}_0+\vec{r}_1)\right]} d\vec{r}_0 d\vec{r}_1.$$

B contains all the contributions to the phase differences that do not depend on the roughness. With $\vec{x}=\vec{r}_1-\vec{r}_0$, $\vec{y}=\vec{r}_1+\vec{r}_0$ the intensity becomes:

$$\langle I(\vec{r})\rangle = \iint e^{iB} e^{-\frac{1}{2}\left\langle|\varphi(\vec{r}_0)-\varphi(\vec{r}_1)|^2\right\rangle} e^{2ia\vec{x}\cdot(\vec{r}-\vec{y}/2)} d\vec{x}d\vec{y}\,, \tag{16}$$

where the integration is over the sample area. Thus the remaining task is to compute $\left\langle|\varphi_0(\vec{r}_0)-\varphi_0(\vec{r}_1)|^2\right\rangle$.

Using the Fourier transforms $\langle h_i(k)h_i(q)\rangle = \delta_{k,-q}\left\langle|h_i(k)|^2\right\rangle$ it follows (see appendix) that the zeroth order contribution is given by:

$$\left\langle|\varphi_0(\vec{r}_0)-\varphi_0(\vec{r}_1)|^2\right\rangle = \tag{17}$$
$$\frac{8}{\pi^2}M_0^2\int_{-\infty}^{\infty}\frac{k_x^2 d\vec{k}}{k^4}\sin^2(\vec{k}.(\vec{r}_0-\vec{r}_1)/2)\left\langle|h_1(k)|^2\right\rangle.$$

It is important to realize that $\left\langle|h_1(k)|^2\right\rangle$ does not depend on $\vec{k}$ and in the case of isotropic self-affine surfaces $\left\langle|h_1(k)|^2\right\rangle$ is represented by [23]:

$$\left\langle|h_1(k)|^2\right\rangle = \frac{A}{32\pi^5}\frac{\alpha\xi^2 w^2}{(1+\xi^2k^2)^{1+\alpha}}, \tag{18}$$

where w describes the amplitude of the fluctuations of the height, ξ is the lateral correlation length within which the surface height of any two points are correlated. The roughness exponent α (with $0\le\xi\le 1$) describes how wiggly the surface is. It turns out that for α=1/2 (see appendix) and α=1 analytical expressions can be obtained for the phase difference. For α=1/2 the equation reads:

$$\left\langle|\varphi_0(\vec{r}_0)-\varphi_0(\vec{r}_1)|^2\right\rangle = \tag{19}$$
$$\frac{A}{8\pi^6}M_0^2\xi^2w^2\left\{\begin{array}{l}\left[-1+e^{-\frac{r}{\xi}}+\gamma+\ln\frac{r}{\xi}+\Gamma(0,\frac{r}{\xi})\right]+\\ \frac{1}{2}\left(\frac{r}{\xi}\right)^{-2}\left(-6+\left(\frac{r}{\xi}\right)^2+2e^{-\frac{r}{\xi}}\left[3+3\frac{r}{\xi}+\left(\frac{r}{\xi}\right)^2\right]\right)\end{array}\right\},$$

where $r=|\vec{r}_0-\vec{r}_1|$. $\Gamma(0,r/\xi)$ is the incomplete gamma function and γ is Euler's constant. Series expansion yields the leading term in $|\vec{r}_0-\vec{r}_1|^2/\xi^2$:

$$\left\langle|\varphi_0(\vec{r}_0)-\varphi_0(\vec{r}_1)|^2\right\rangle \approx \tag{20}$$
$$\frac{A}{8\pi^6}M_0^2w^2\left\{\frac{1}{4}|\vec{r}_0-\vec{r}_1|^2-\frac{1}{9}\frac{|\vec{r}_0-\vec{r}_1|^3}{\xi}\right\}.$$

For the first-order term, the phase difference is derived as (see Eq.(13)) :

$$\frac{1}{z_1}\left[\varphi_1(\vec{r}_0)-\varphi_1(\vec{r}_1)\right] = \frac{2M_0(y_0-y_1)Ad}{z_1} + \tag{21}$$
$$\frac{2M_0(y_0-y_1)}{z_1}\int\int_A dx'dy'\left[h_1(x',y')+h_0(x',y')\right].$$

The first term to the right leads to a factor B in Eq. (16) and the Gaussian average becomes (α=1/2):

$$\frac{1}{z_1^2}\left\langle|\varphi_1(\vec{r}_0)-\varphi_1(\vec{r}_1)|^2\right\rangle = \tag{22}$$
$$\frac{8M_0^2(y_0-y_1)^2}{z_1^2}\int\int_A d\vec{r}d\vec{r}'\int_{-\infty}^{\infty}\int d\vec{k}e^{i\vec{k}.(\vec{r}-\vec{r}')}\left\langle|h(k)|^2\right\rangle$$

or:

$$\frac{1}{z_1^2}\left\langle|\varphi_1(\vec{r}_0)-\varphi_1(\vec{r}_1)|^2\right\rangle \propto \frac{w^2\xi^2(y_0-y_1)^2M_0^2}{2z_1^2}. \tag{23}$$

4. DISCUSSION AND CONCLUSIONS

In the theoretical analysis it was explicitly assumed that the magnetization lies exclusively in one direc-

tion, i.e. $\vec{M}(\vec{r}') = M_0 \hat{e}_x$. A uni-axial anisotropy is induced during film deposition due to an applied magnetic field and due to the random orientations of the grains in nano-crystalline material, and indeed the magnetocrystalline anisotropy is averaged out to a large extent. Nevertheless, in nano- (and polycrystalline) soft magnetic films with an induced uniaxial anisotropy, the direction of the magnetization wiggles around the easy axis producing a so-called micromagnetic ripple [8]. The local variation of the magnetic field in a thin film influences the out-of-focus image in the transmission electron microscopy via variation of the Lorentz force that acts perpendicular to the directions of the electron beam and the magnetic induction. Consequently, in Lorentz transmission electron microscopy the quasi-periodic oscillation of the transversal component of the local magnetization leads to almost parallel (1D) fringes in under- or over-focused images. This phenomenon is clearly visible in Figs. 3 and 5. In the classical theory of the LTEM imaging of micromagnetic ripple [6] and in a diffraction approach [21] the oscillations are one-dimensional and the absolute value of the magnetization has been assumed to be constant. From the spacing between the fringes the wavelength and the amplitude of the angular spread of the magnetization direction can be estimated using a simplified relation [15]. The exchange interaction reduces the angular spread of the magnetization vector due to the local residual crystalline anisotropy, leading to a correlated wiggling of the magnetization around the easy axis (EA) producing the ripples observed in Lorentz microscopy. This wiggling can be characterized by an amplitude of the transversal component of the magnetization, $\Delta M_y(x)$, which is a periodic function in x-direction, i.e. *perpendicular* to the ripples, with a wavelength λ_x = 0.22 ±0.02 mm in Fig. 3. A transversal oscillation $\Delta M_y(y)$ is energetically unfavorable [6]. Additionally, the intensity of the image is also rather inhomogeneous *along* the ripple direction, seen as a dotted contrast in Figs. 3 and 5. This variation cannot be explained by oscillations along the longitudinal direction of the transverse component of the magnetization but requires a variation of the magnetization along the main direction, ΔM_x, i.e. an oscillation of the longitudinal component of magnetization. The periodicity of this mode λ_y lies experimentally between 0.11 and 0.12 mm (Fig. 3). These effects can be included in the vector potential formulation (see Eq.(5)) by adding $\Delta M_x(y)$ and $\Delta M_y(x)$. Assuming a simple harmonic oscillation $M_0(y\text{-}y')$ in Eq.(9) has to be replaced by:

$$\left(M_0 + \Delta M_{0x} \sin\frac{2\pi y}{\lambda_y} \right)(y - y') - (x - x')\Delta M_{0y} \sin\frac{2\pi x}{\lambda_x}. \tag{24}$$

If we take into account Eq. (24), the theoretical analysis becomes more complicated and undoubtedly analytical expressions cannot be easily attained. These aspects are subject of future investigations.

In this paper, we did not pursue the goal to reproduce the experimental images, but to find analytical relations between phase maps in electron holography and intensity maps in Lorentz transmission electron microscopy including the thickness variation over the sample. For particular statistical description of the roughness and values for the roughness it was shown that analytical expressions could be obtained. We have demonstrated that starting from the concept of the vector potential in classical electrodynamics these results can be achieved by assuming independent Gaussians and translational invariance for the height correlation functions.

ACKNOWLEDGEMENTS

The authors are indebted to Prof. N. Chechenin, Dr. T. Vystavel, Daan Hein Alsem for the TEM operation and discussions, Dr. A.R. Chezan for the film deposition and Dr. G. Palasantzas for the AFM observations. This work was supported by the Netherlands Foundation for Applied Research (STW-Utrecht), the Prioriteitsprogramma Materialenonderzoek (PPM) and the Netherlands Institute for Metals Research.

APPENDIX

In this appendix Eq.(17) and Eq.(19) are derived starting from Eq.(12) that directly follows from Eq.(10). Because

$$\frac{y - y'}{(x - x')^2 + (y - y')^2} = \frac{1}{2\pi} \int_{-\infty}^{\infty} \int dpdq \; e^{i(px+py)} \frac{p}{p^2 + q^2} \tag{A1}$$

the expression of the zero-th order contribution (in $1/z_1$) to the phase becomes

$$\varphi_0(x,y) = \frac{1}{\pi} M_0 \int_A \int dx'dy' \int_{-\infty}^{\infty} dk_x dk_y e^{ik_x(x-x')} e^{ik_y(y-y')} \frac{k_x}{k_x^2 + k_y^2} \{d + h_1(x',y') + h_0(x',y')\} \quad \text{(A2)}$$

or:

$$\varphi_0(\vec{r}) = \frac{1}{\pi} M_0 \int_{-\infty}^{\infty} \int d\vec{k} \frac{k_x}{k^2} e^{i\vec{k}.\vec{r}} \int_A d\vec{r}' e^{-i\vec{k}.\vec{r}'} \{d + h_1(\vec{r}') + h_0(\vec{r}')\} \quad \text{(A3)}$$

or:

$$\varphi_0(\vec{r}) = \frac{1}{\pi} M_0 \int_{-\infty}^{\infty} \int \frac{k_x d\vec{k}}{k^2} e^{i\vec{k}.\vec{r}} \{Ad\delta_{r,0} + h_1(\vec{k}) + h_0(\vec{k})\}. \quad \text{(A4)}$$

Here, $h_0(\vec{r})$ and $h_1(\vec{r}')$ are independent Gaussians and $\langle h_i(\vec{r}) h_i(\vec{r}') \rangle = \langle h_i(\vec{r} - \vec{r}') h_i(0) \rangle$ with Fourier transform $\langle h_i(k) h_i(q) \rangle = \delta_{k,-q} \langle |h_i(k)|^2 \rangle$. The only restriction we make is that the amplitude of the fluctuations $|h_i(\vec{r})| < d/2$. The phase difference (Gaussian average) becomes:

$$\langle |\varphi_0(\vec{r}_0) - \varphi_0(\vec{r}_1)|^2 \rangle = \frac{1}{\pi^2} M_0^2 \int_{-\infty}^{\infty} \iiint \frac{k_x d\vec{k}}{k^2} \frac{q_x d\vec{q}}{q^2} (e^{\vec{k}.\vec{r}_0} - e^{\vec{k}.\vec{r}_1})(e^{\vec{q}.\vec{r}_0} - e^{\vec{q}.\vec{r}_1}) (\langle h_1(k) h_1(q) + h_0(k) h_0(q) \rangle) \quad \text{(A5)}$$

or:

$$\langle |\varphi_0(\vec{r}_0) - \varphi_0(\vec{r}_1)|^2 \rangle = \frac{8}{\pi^2} M_0^2 \int_{-\infty}^{\infty} \frac{k_x^2 d\vec{k}}{k^4} \sin^2(\vec{k}.(\vec{r}_0 - \vec{r}_1)/2) \langle |h_1(k)|^2 \rangle. \quad \text{(A6)}$$

We take $f(k) = \langle |h_1(k)|^2 \rangle$, $\vec{r} = \vec{r}_0 - \vec{r}_1 = r(\cos\chi, \sin\chi)$ and $\vec{k} = k(\cos\theta, \sin\theta)$. Then Eq.(A6) can be recast in:

$$\langle |\varphi_0(\vec{r}_0) - \varphi_0(\vec{r}_1)|^2 \rangle = \frac{8}{\pi} M_0^2 \int_0^{\infty} dk \int_0^{2\pi} d\theta \frac{\cos^2\theta}{k} [1 - \cos(kr\cos(\theta - \chi))] f(k) \quad \text{(A7)}$$

Using the relationship

$$\cos(kr\cos(\theta - \chi)) = J_0(kr) + 2\sum_{n=1}^{\infty} (-1)^n J_{2n}(kr) \cos(2n(\theta - \chi))$$

it follows that

$$\langle |\varphi_0(\vec{r}_0) - \varphi_0(\vec{r}_1)|^2 \rangle = \frac{8}{\pi} M_0^2 \int_0^{\infty} dk [1 - J_0(kr) + J_2(kr)\cos 2\chi] \frac{f(k)}{k}. \quad \text{(A8)}$$

$f(k)$ takes the form:

$$f(k) = \frac{a}{(k^2 + b^2)^{1+\alpha}}, \quad \text{(A9)}$$

where α refers to the roughness exponent.

With $k = U/r$ and $r \neq 0$ and $b = 1$

$$\langle |\varphi_0(\vec{r}_0) - \varphi_0(\vec{r}_1)|^2 \rangle = \frac{8}{\pi} M_0^2 a r^{2(1+\alpha)} \int_0^{\infty} du \left[\frac{1 - J_0(u) + J_2(u)\cos 2\chi}{u} \right] \frac{1}{(u^2 + r^2)^{1+\alpha}}, \quad \text{(A10)}$$

where $J_n(u)$ is the Bessel function of the first kind. For an isotropic self-affine roughness $f(k)$ is described as [23]:

$$f(k) = \frac{A}{32\pi^5} \frac{\alpha \xi^2 w^2}{(1 + \xi^2 k^2)^{1+\alpha}}, \quad \text{(A11)}$$

where w is the amplitude of the fluctuations of the height, ξ is the lateral correlation length within which the surface height of any two points are correlated. The roughness exponent α (with $0 \leq \alpha \leq 1$) describes how wiggly the surface is.

For $\alpha = 1/2$, $\chi = 0$ an analytical expression can be found:

$$\langle |\varphi_0(\vec{r}_0) - \varphi_0(\vec{r}_1)|^2 \rangle = \frac{A}{8\pi^6} M_0^2 \xi^2 w^2 \left\{ \begin{array}{l} \left[-1 + e^{-\frac{r}{\xi}} + \gamma + \ln\frac{r}{\xi} + \Gamma\left(0, \frac{r}{\xi}\right) \right] + \\ \frac{1}{2}\left(\frac{r}{\xi}\right)^{-2} \left(-6 + \left(\frac{r}{\xi}\right)^2 + 2e^{-\frac{r}{\xi}} \left[3 + 3\frac{r}{\xi} + \left(\frac{r}{\xi}\right)^2 \right] \right) \end{array} \right\} \quad \text{(A.12)}$$

with $r = |\vec{r}_0 - \vec{r}_1|$.

For $\alpha = 1$ we find

$$\left\langle \left|\varphi_0(\vec{r}_0) - \varphi_0(\vec{r}_1)\right|^2 \right\rangle =$$

$$\frac{A}{4\pi^6} M_0^2 \xi^2 w^2$$

$$\left(-\frac{1}{2} + K_0(\frac{r}{\xi}) + \frac{1}{2}\frac{r}{\xi} K_1(\frac{r}{\xi}) + \ln(\frac{r}{\xi}) - 4\left(\frac{\xi}{r}\right)^2 \right.$$

$$\left. + \frac{1}{2}\frac{r}{\xi} K_3(\frac{r}{\xi}) \right) \quad \text{(A13)}$$

where $K_n(r/\xi)$ represents the modified Bessel function of the second kind.

REFERENCES

[1] Y.P. Zhao, G-C. Wang and T.M. Lu, *Experimental Methods in the Physical Sciences*, Vol. 37 (Academic Press, New York, 2000).

[2] R.M. Jeong // *IEEE Trans.Magn.* **24**(1988) 1725.

[3] G. Fishman and D. Calecki // *Phys. Rev. B* **43** (1991) 11581.

[4] T. Schuhrke, J. Zweck and H. Hoffmann// *Ultramicroscopy* **58** (1995) 319.

[5] P.J. Grundy and R.S. Tebble // *Advances in Physics* **17** (1968) 153.

[6] H.W. Fuller and M.E. Hale // *J. Appl. Phys.* **31** (1960) 238.

[7] M. De Graef, In: *Experimental Methods in the Physical Sciences, Volume 36: Magnetic Imaging and its Applications to Materials*, ed. by M. De Graef and Y. Zhu (Academic Press, N.Y., 2000) p.27.

[8] H. Hoffmann // *J. Appl. Phys*. **35** (1964)1790.

[9] D. Gabor //*Proceedings of the Royal Society A* **197** (1949) 454.

[10] A. Tonomura, *Electron Holography, Springer Series in Optical Sciences* (Berlin, Germany, 1999).

[11] E. Völkl, L. F. Allard and D. C. Joy, *Introduction to electron holography* (Kluwer, New York, 1999).

[12] Jeff Th.M. De Hosson, Nicolai G. Chechenin, Daan Hein Alsem, Tomas Vystavel, Bart Kooi, Antoni Chezan and Dik Boerma // *Microscopy and Microanalysis* **8** (2002) 274.

[13] N.G.Chechenin, J.Th.M. De Hosson and D.O. Boerma // *Philos. Magazine* **83** (2003) 2899.

[14] A.R. Chezan , C.B. Craus, N.G. Chechenin, L. Niesen and D.O. Boerma // *Physica Status Solidi* **189** (2002) 833.

[15] N.G. Chechenin, A.R. Chezan, C.B. Craus, T.Vystavel, D.O. Boerma, J.Th.M. De Hosson and L. Niesen // *J. Magn. Magn. Mater*. **242-245** (2002) 180 .

[16] N.G. Chechenin, C.B. Craus, A.R. Chezan T.Vystavel, D.O. Boerma, J.Th.M. De Hosson and L. Niesen // *IEEE Trans Act*. **38** (2002) 3027 .

[17] J.M. Chapman // *J. Phys. D: Appl. Phys*. **17** (1984) 623.

[18] L. Reimer, *Transmission Electron Microscopy. Physics of Image Formation and Microanalysis, Springer Series in Optical Sciences* (Springer-Verlag, Berlin, 1989).

[19] J. Cowley // *Ultramicroscopy* **41** (1992) 335.

[20] Y. Aharonov and D. Bohm // *Phys. Rev*. **115** (1958) 485.

[21] D. Wohlleben // *J.Appl.Phys.* **38** (1967) 3341.

[22] J.D. Jackson, *Classical Electrodynamics* (Wiley, New York, 1975).

[23] Y.P. Zhao, G. Palasantzas, G.C. Wang and J.Th.M. De Hosson // *Phys.Rev. B* **60** (1999) 1216 .